


Cite this: *RSC Adv.*, 2025, 15, 15384

Molecular design and performance of emissive amide-containing compounds as corrosion inhibitors: synthesis, electrochemical evaluation, DFT calculations and molecular dynamics simulations†

Abdelreheem A. Saddik,^{†ab} Mostafa Sayed,^{†*c} Ahmed A. K. Mohammed,^a Mohamed Abdel-Hakim^d and Mostafa Ahmed^{bc}

Corrosion presents a significant challenge across various industries, resulting in considerable economic losses and safety risks. Organic compounds that contain aryl moieties and hetero atoms like nitrogen and oxygen have potential applications as efficient inhibitors and coating layers for the surface of metals. Herein, we investigate the corrosion inhibition of mild steel in 1.0 M H₂SO₄ using newly synthesized amide-containing compounds with naphthalene (**naphthamide 6C–9C**) or benzene (**benzamide 6C–9C**) structures. Characterization of these inhibitors *via* IR and NMR spectroscopy confirmed their chemical structures. Electrochemical analyses, including open circuit potential and potentiodynamic polarization tests, showed that these compounds significantly reduce the corrosion rate of mild steel. They achieved inhibition efficiencies up to 80% at optimal concentrations. The enhanced performance of these inhibitors is linked to their greater molecular weight and longer alkyl chains, which improve adsorption and surface coverage. Photophysical investigations revealed notable solvatochromic effects and red shifts in polar solvents, indicating strong interactions with the environment. Density Functional Theory (DFT) calculations provided further insights into the molecular structure, electronic distributions, and adsorption behavior, confirming the higher efficiency of series **naphthamide 6C–9C** compared to **benzamide 6C–9C**. Moreover, molecular Dynamics (MD) simulations corroborated the formation of stable protective layers on the metal surface. From the DFT calculations it is evidently that **naphthamide 9C** exhibited a smaller HOMO–LUMO energy gap compared to compound **benzamide 9C**, indicating higher reactivity and greater inhibitory efficiency. The integration of experimental and theoretical findings confirms that amide-containing naphthalene and benzene derivatives are highly effective corrosion inhibitors, suitable for industrial applications.

Received 10th February 2025
Accepted 2nd May 2025

DOI: 10.1039/d5ra00978b

rsc.li/rsc-advances

1. Introduction

Corrosion is a prevalent issue affecting various industries, leading to significant economic losses and safety concerns.^{1–3} Mild steel, widely used in construction, automotive, and chemical industries, is particularly susceptible to corrosion in acidic environments,^{4–6} such as sulfuric acid (H₂SO₄). The development of effective

corrosion inhibitors is therefore critical to prolong the lifespan of mild steel and enhance its performance in corrosive environments.^{7,8} Corrosion inhibitors are substances that, when added in small concentrations, effectively reduce the corrosion rate of metals.⁹ Among the various types of corrosion inhibitors, organic compounds have gained significant attention due to their high efficiency and environmental compatibility.^{10–15} These compounds typically contain heteroatoms such as nitrogen, oxygen, and sulfur, which can donate electrons to the metal surface, forming a protective film that hinders the corrosion process.¹⁵

Amide-containing compounds have emerged as promising corrosion inhibitors^{16–20} due to their ability to form stable complexes with metal surfaces.^{20,21} The presence of amide groups enhances adsorption through electron donation,^{22,23} while aromatic moieties, such as naphthalene and benzene, contribute to the stability and effectiveness of the inhibition process. The synergistic effect of these functional groups can lead to the development of

^aDepartment of Chemistry, Faculty of Science, Assiut University, Assiut 71516, Egypt

^bInnovation Incubation Center, National Tsing Hua University, Hsinchu, 300, Taiwan

^cChemistry Department, Faculty of Science, New Valley University, El-Kharja 72511, Egypt. E-mail: mostafaali@mail.ustc.edu.cn; mostafasayed@sci.nvu.edu.eg; drmostafa@scinv.au.edu.eg

^dDepartment of Chemistry, Faculty of Science, Al-Azhar University, Assiut 71524, Egypt

† Electronic supplementary information (ESI) available. See DOI: <https://doi.org/10.1039/d5ra00978b>

‡ These authors contributed equally to this work (Abdelreheem A. Saddik and Mostafa Sayed).



highly efficient corrosion inhibitors.^{24,25} Naphthalene and benzene derivatives have been extensively studied for their corrosion inhibition properties.^{26–28} Naphthalene-based compounds are known for their planar structure, which facilitates strong π - π interactions with the metal surface.^{29,30} Benzene derivatives, on the other hand, offer versatility in functionalization, allowing for the fine-tuning of their inhibitory properties.^{31–34} Incorporating naphthalene or benzene moieties with amide bond into a single compound could potentially enhance corrosion inhibition through combined adsorption mechanisms and electronic effects.^{28,35}

Amide-containing aromatic compounds have garnered significant interest in the field of metal sensing due to their unique electronic and structural characteristics.^{35–39} The presence of amide groups, coupled with aromatic moieties such as naphthalene and benzene, imparts distinct photophysical properties,⁴⁰ including strong absorption and emission profiles that are highly sensitive to their chemical environment.⁴¹ These properties enable the compounds to exhibit notable solvatochromism and fluorescence, making them excellent candidates for various sensing applications.^{42–45} Specifically, the ability of these compounds to form stable complexes with metal ions through coordination interactions allows them to act as effective metal sensors.^{46–49} This dual functionality of strong photophysical response and selective metal ion recognition positions amide-containing aromatic compounds as promising materials for developing advanced sensors for environmental monitoring, biological imaging, and industrial applications.^{50–52}

In this study, we synthesized a series of amide-containing compounds with naphthalene and benzene moieties and evaluated their corrosion inhibition performance on mild steel in 1.0 M H₂SO₄. The synthesized inhibitors were characterized using various spectroscopic techniques to confirm their chemical structures. The corrosion inhibition efficiency was assessed through potentiodynamic polarization studies. Additionally, the photophysical properties of the inhibitors were investigated to understand their electronic behavior and interaction with the metal surface. To gain deeper insights into the inhibition mechanism, density functional theory (DFT) calculations were performed. DFT calculations provide valuable information on the molecular structure, electronic distribution, and adsorption behavior of the inhibitors on the mild steel surface. By

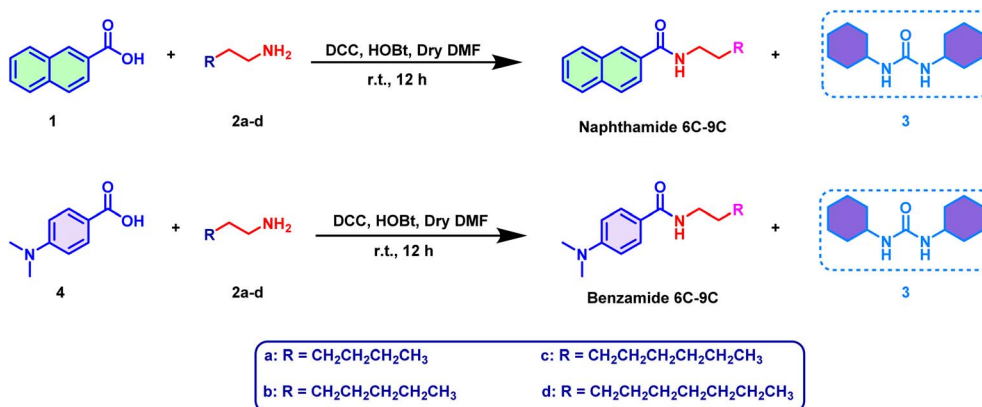
correlating experimental results with theoretical calculations, we aimed to elucidate the factors contributing to the corrosion inhibition efficiency of the synthesized compounds. This comprehensive study not only highlights the potential of amide-containing naphthalene and benzene derivatives as effective corrosion inhibitors but also provides a detailed understanding of their interaction mechanisms with mild steel in acidic environments. The findings from this research could pave the way for the development of new, highly efficient, and environmentally friendly corrosion inhibitors for industrial applications.

2. Results and discussions

2.1. Synthesis of the target compounds

The synthesis of the target amide compounds, *N*-alkyl-2-naphthamides (**naphthamide 6C–9C**) and 4-(dimethylamino)-*N*-alkylbenzamides (**benzamide 6C–9C**), was efficiently accomplished using a well-established amide coupling strategy. This process involved the reaction of either naphthanoic acid **1** or 4-dimethylamino benzoic acid **4** with various primary aliphatic amines **2a–d** namely, hexyl amine, heptyl amine, octyl amine, and nonyl amine. The choice of DCC as a coupling agent and HOBT as an organic additive in dry DMF solvent provided an optimal environment for the formation of the amide bond containing products. The amide coupling reaction proceeded *via* the formation of a reactive *O*-acylisourea intermediate from the carboxylic acid in the presence of DCC. This intermediate subsequently reacts with the primary amine to form the desired amide product, releasing dicyclohexylurea **3** (DCU) as a by-product (Scheme 1). HOBT was employed to improve the reaction efficiency and reduce the formation of side products by stabilizing the *O*-acylisourea intermediate (Scheme S1†). The thermal stability of the synthesized compounds was attributed to the rigid aryl moieties present in their structures. This rigidity likely contributed to the robustness of the amide linkage, ensuring the compounds maintained their integrity under various conditions.

The obtained amide inhibitors were characterized using various spectroscopic techniques such as IR and NMR, to confirm their structures and purity. The FTIR spectra of the synthesized amides displayed characteristic absorption bands corresponding



Scheme 1 Pathway for synthesis of the target products.



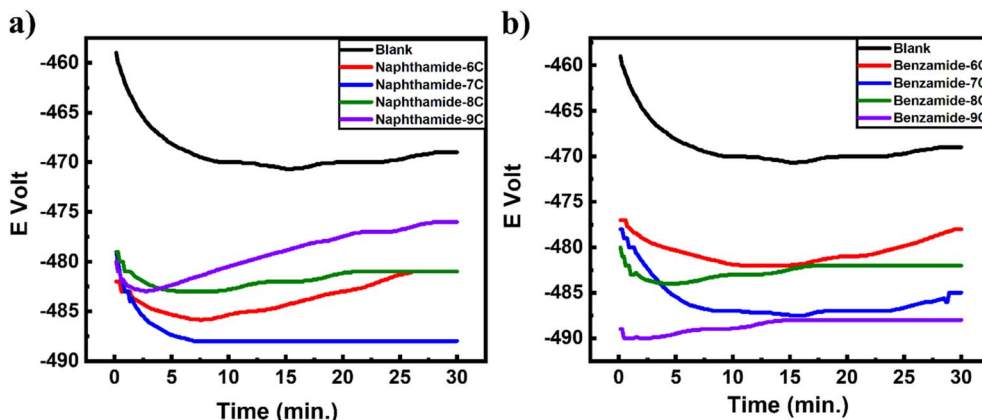


Fig. 1 Potential–time curves of mild steel with the amid compounds: (a) naphthamide 6C–9C and b) benzamide 6C–9C.

to NH and C=O functional groups. For example, compound **naphthamide 6C** exhibited NH stretching vibrations around 3408 cm^{-1} and 3323 cm^{-1} , and a strong C=O stretching vibration at 1625 cm^{-1} . Additionally, the spectra showed bands in the $2932\text{--}2858\text{ cm}^{-1}$ range, indicative of aliphatic C–H stretching. The ^1H NMR spectra revealed signals attributable to both aromatic and aliphatic protons, confirming the formation of the amide bond. For instance, compound **naphthamide 6C** displayed a singlet at 8.61 ppm for the NH proton, along with multiplets in the aliphatic region for the CH_2 and CH_3 groups. Similarly, the ^{13}C NMR spectra showed a distinctive signal for the carbonyl carbon (CONH) around 166.08 ppm, alongside signals for the aliphatic carbons. The structures of all other amide products **naphthamide 7C–9C** and **benzamide 6C–9C** were confirmed in the same manner with product **naphthamide 6C** which showed good agreement with the claimed structures. The reaction conditions employed, including room temperature and the use of dry DMF, facilitated high-yielding reactions with minimal side product formation. The white precipitate of DCU was easily removed by filtration, simplifying the purification process. Recrystallization from dilute ethanol provided the final products in high purity. The synthesis of *N*-alkyl-2-naphthamides and 4-(dimethylamino)-*N*-

alkylbenzamides was effectively achieved through a DCC/HOBt-mediated coupling reaction. The process yielded structurally confirmed and thermally stable amide compounds, showcasing the reliability and efficiency of this synthetic approach for producing high-purity amides suitable for further applications. All FTIR and NMR spectra can be found in the ESI (Fig. S1–S24†).

2.2. Electrochemical studies

2.2.1 Open circuit potential OCP. Fig. 1 and 2 show the curves of E (mV) against time (min) at zero current for MS immersed in both the blank solution and a 200 ppm concentration of the tested inhibitors (amide compounds **naphthamide 6C–9C** and **benzamide 6C–9C**). It is evident that for blank solution curves, the steady-state potential ($E_{s,s}$) shifts to a more negative potential than the immersion potential E_{im} ; this shift is ascribed to the degradation of the oxide coating from the surface of the metal substrate until it attains $E_{s,s}$ of the corrosion cell. When different concentrations of the testing inhibitors were added, the $E_{s,s}$ value shifted more toward the positive potential than it did in the blank solution. This impact results from the creation of an adsorbed layer of inhibitor

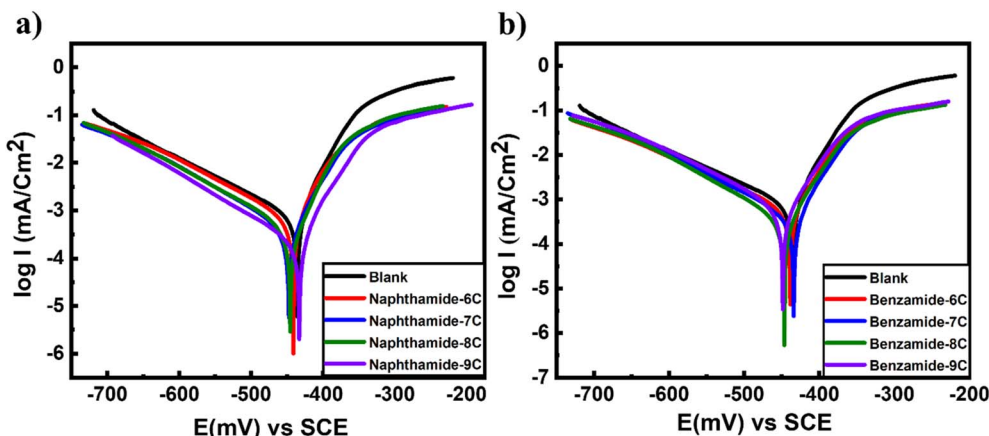


Fig. 2 Tafel plots polarization curves of mild steel exposed to different inhibitors at 200 ppm for amide compounds: (a) naphthamide 6C–9C and (b) benzamide 6C–9C.



Table 1 Potential (mV) against time (min) of mild steel exposed to 1.0 M H₂SO₄ with amide compounds^a

Inhibitors	$-E_{im}$	$-E_{s,s}$
Blank	459	469
Naphthamide 6C	482	481
Naphthamide 7C	479	488
Naphthamide 8C	479	481
Naphthamide 9C	480	476
Benzamide 6C	477	478
Benzamide 7C	478	485
Benzamide 8C	480	509
Benzamide 9C	489	488

^a Where: $E_{s,s}$ is the steady-state potential, E_{im} is the immersion potential (E_{im}).

molecules on the active sites of the MS surface. Data obtained from OCP is presented in Table 1.

2.2.2 Tafel polarization. Fig. 1 and 2 illustrate the potentiodynamic polarization curves displaying the corrosion of mild steel in a 1.0 M H₂SO₄ solution, both before and after to the addition of the examined inhibitors. The presence of amide derivatives **naphthamide 6C–9C** and **benzamide 6C–9C** induces shifts in Tafel slopes (Fig. 1 and 2). This indicated that: (i) the adsorption of inhibitor molecules on the surface of MS electrodes and (ii) the E_{corr} of the utilized inhibitors varies positively from that of the blank solution, with the difference not exceeding 85 mV, thereby demonstrating that these inhibitors are mixed-type, resulting in a reduction of both anodic and cathodic Tafel slopes.⁵³ Table 2 presents the metrics derived from TF, including I_{corr} , E_{corr} , CR, IE%, and θ of MS, both with and without inhibitors. In the absence of analyzed inhibitors, I_{corr} rises to 2699 ($\mu\text{A cm}^{-2}$) and CR ascends to 2488 mpy. Furthermore, Fig. 2 shows the Tf plots of the effect of amide compounds (200 ppm of **naphthamide 6C–9C** and **benzamide 6C–9C**) on the mild steel in 1.0 M sulfuric acid. Compounds (**naphthamide 6C–9C**) give close corrosion inhibition, and the same behavior is exhibited by compounds (**benzamide 6C–9C**) with corrosion inhibition in the range of 80% and 75% respectively (Table 2). The higher inhibition efficiency of (**naphthamide 6C–9C**) than (**benzamide 6C–9C**) compounds attributed to the higher molecular weight of the compounds (**naphthamide 6C–9C**) compared to (**benzamide 6C–**

9C) compounds and the chain length plays a role in the inhibition causing a slight change among compounds for every group, which promotes higher inhibition and higher surface area coverage of the metal.^{54–56} These results completely agreed with the results of theoretical quantum chemistry calculations that were performed, which investigated that there is no difference in the energy gap between compounds in the same group (**naphthamide 6C–9C** and **benzamide 6C–9C**). Moreover, the observed trend in inhibition efficiency can be interpreted by a precious look over structural aspects of investigated compounds. Generally, all naphthalene moiety containing inhibitors exhibit a greater inhibition efficiency than that of corresponding phenyl derived inhibitors. This might be attributed to the fact that naphthalene moiety has an extended planar aromatic system with delocalized pi electrons, this contributes to greater interaction with metallic iron, resulting in a greater surface coverage and hence greater protection. Meanwhile, the hydrophobic tail can be oriented towards the solution which might repel polar corrosive species from further attack on metal surface.

As shown in Table S1,[†] our one-step synthesized amides demonstrate inhibition efficiency comparable to that of various established corrosion inhibitors. Unlike these alternatives, which often require multi-step syntheses and costly solvents, our amides offer a more economical option without compromising protective performance. Considering the advantages of the ease synthesis and one-pot strategy of our current study over the other reported methods, this technique offers a straightforward and effective strategy for the obtaining of new inhibitors.

2.3. Photophysical study

The absorption spectra of compounds **naphthamide 6C–9C** and **benzamide 6C–9C** were recorded in various solvents (DCM, EtOH, THF, dioxane, ACN, DMF, and DMSO) at room temperature. The absorption maxima of compounds **naphthamide 6C–9C** in various solvents at concentration 100 μM showed λ_{max} at 281 nm confirmed with the absorption maxima of the naphthalene moiety in different organic solvents with little red-shift to 2–3 nm by changing the solvents (Fig. S24[†]).⁵⁷ Furthermore, compounds **benzamide 6C–9C** at concentration 100 μM exhibited an absorption band at $\lambda_{max} = 287$ nm in THF, characteristic of the 4-dimethylaminobenzamide moiety.⁵⁸ However, these compounds displayed a solvatochromic effect in their absorption spectra, with a red shift observed in various solvents ranging from 289 nm to 294 nm and reaching 301 nm in EtOH, which can be attributed to the increased stabilization of the excited state relative to the ground state by polar solvents. This reduction in the energy gap between the excited and ground states leads to the observed bathochromic shift (Fig. 3, S24 and S25[†]).⁵⁹

Furthermore, the fluorescence emission of compounds **naphthamide 6C–9C** and **benzamide 6C–9C** was examined in various organic solvents. Compounds **naphthamide 6C–9C** exhibited a red shift in their emission spectra, ranging from 350 to 355 nm compared to the 334 nm emission in THF, as solvent polarity increased. Notably, these compounds displayed the strongest emission in ethanol. Similarly, compounds

Table 2 Potentiodynamic polarization parameters of mild steel immersed in 1.0 M H₂SO₄ with amide compounds

Inhibitors	I ($\mu\text{A cm}^{-2}$)	C.R	IE%	θ
Blank	2699	2488.57	—	—
Naphthamide 6C	576.2	531.277	80.316	0.8032
Naphthamide 7C	574.1	529.341	80.388	0.8039
Naphthamide 8C	573.1	528.419	80.422	0.8042
Naphthamide 9C	570.2	525.745	80.521	0.8052
Benzamide 6C	724.9	668.384	75.236	0.7524
Benzamide 7C	723.4	667.001	75.287	0.7529
Benzamide 8C	720.2	664.05	75.396	0.754
Benzamide 9C	719.1	663.036	75.434	0.7543



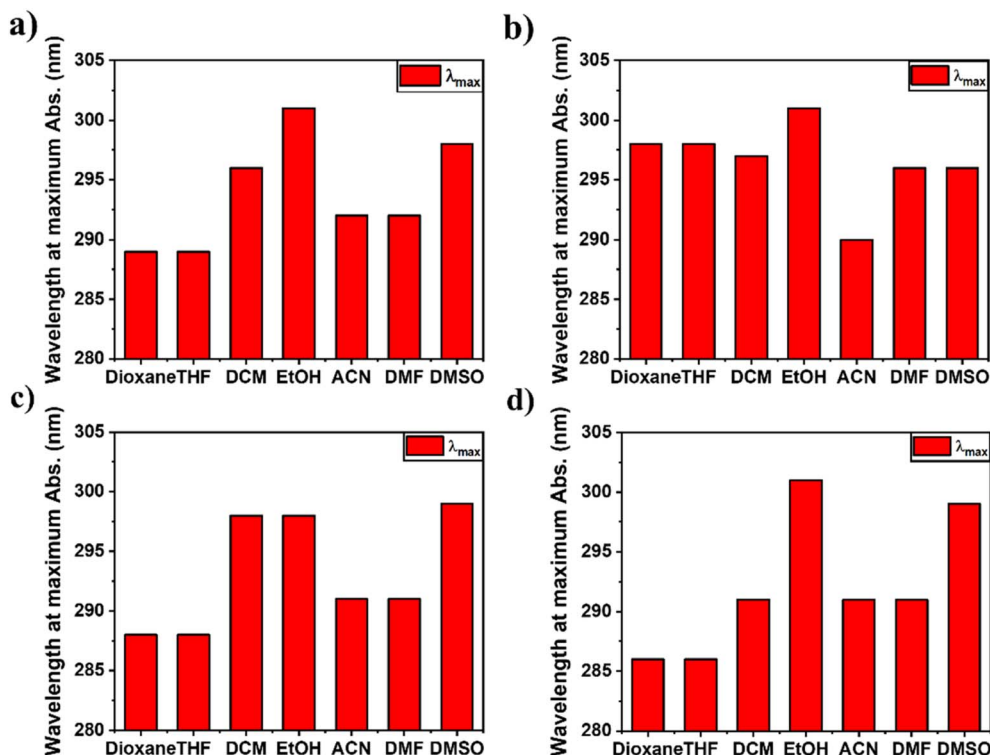


Fig. 3 (a–d) The relation between the wavelength at maximum absorption of compounds **6a–d** at different organic solvents (dioxane, THF, DCM, EtOH, ACN, DMF, and DMSO) at 100 μM ; (a) benzamide **6C**, (b) benzamide **7C**, (c) benzamide **8C**, and (d) benzamide **9C**.

benzamide 6C–9C demonstrated a red shift in emission spectra (351–363 nm) compared to dioxane (348 nm), with pronounced fluorescence. Interestingly, dual emission at 450 nm was observed in more polar solvents (ethanol, acetonitrile, DMF, and DMSO). This phenomenon could be attributed to either an anomalous emission transition from a dark state or the limited solubility of these compounds in these solvents, especially in acetonitrile (Fig. 4, S26–S28[†]).⁶⁰ Further, the concentration-dependent emission spectra of compounds **naphthamide 6C–9C** were examined in ethanol, while compounds **benzamide 6C–9C** were evaluated in dioxane at different concentrations (5, 10, 50, and 100 μM). As the concentration increased, we observed a corresponding increase in fluorescence intensity without any shift in the emission spectra. This suggests that the compounds' fluorescence properties remain unchanged by concentration changes (Fig. S29[†]).

2.4. Quantum-chemical calculations

2.4.1 DFT and MD simulations. Density functional theory (DFT) calculations were conducted on the eight compounds to elucidate their geometric and electronic structures, provide a molecular-level interpretation of the experimental findings, and uncover the inhibitory mechanisms of molecules **naphthamide 9C** and **benzamide 9C** on the iron (Fe) surface. Fig. 5 displays the optimized structures of compounds **naphthamide 9C** and **benzamide 9C** at the B3LYP-D3(BJ)/6-31G(d) level, accompanied by reduced density gradient (RDG) plots. These plots are instrumental in identifying noncovalent interactions.

Selected geometric parameters and intramolecular forces are also illustrated. For clarity, the full straight-chain alkane segments of both compounds are not fully depicted. In compound **naphthamide 9C**, the torsional angle between the amide group and the naphthalene ring is 45.2°. The green surfaces between the amide group, naphthalene ring, and alkane chain indicate the presence of van der Waals interactions. Similarly, in compound **benzamide 9C**, the torsional angle between the amide group and the dimethylaniline moiety is 19.2°, with van der Waals forces governing the intramolecular interactions. The remaining molecules exhibit comparable geometric parameters, as they differ primarily in the length of their alkane side chains.

Next, the isosurface maps of the highest occupied molecular orbital (HOMO) and lowest unoccupied molecular orbital (LUMO) were computed for all structures at the B3LYP-D3(BJ)/6-31G(d) level to elucidate the electronic structure of these compounds. These calculations reveal the orbital distributions, which are critical for understanding the interaction between the inhibitor molecules and the iron (Fe) surface. The frontier molecular orbitals (FMOs) play a key role in this interaction, as electrons are transferred from the HOMO of the inhibitor to the vacant orbitals of the metal, while the LUMO of the inhibitor accepts electrons from the filled d-orbitals of the metal. Fig. 6 illustrates the HOMO and LUMO distributions, along with their energy differences, for compounds **naphthamide 9C** and **benzamide 9C**. For compound **naphthamide 9C**, both the HOMO and LUMO are localized over the amide group and the



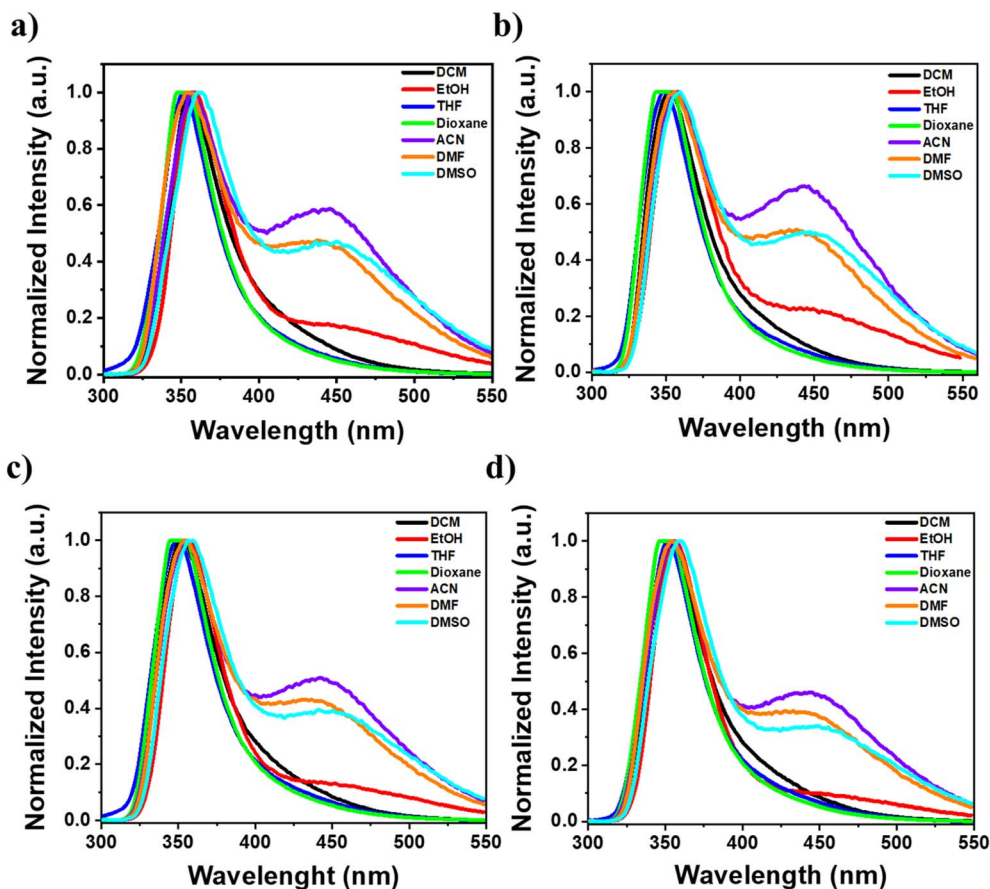


Fig. 4 (a–d) Normalized emission spectra of compounds 6a–d at different organic solvents (DCM, EtOH, THF, dioxane, ACN, DMF, and DMSO) at 100 μM ($\lambda_{\text{ex}} = 287 \text{ nm}$); (a) benzamide 6C, (b) benzamide 7C, (c) benzamide 8C, and (d) benzamide 9C.

naphthalene ring. The HOMO primarily consists of the lone pairs of oxygen (O) and nitrogen (N) atoms, as well as the π orbitals of the aromatic ring, while the LUMO is composed of the π^* orbitals of the aromatic system. The aliphatic side chain does not contribute to either orbital. The HOMO energy is -5.89 eV , the LUMO energy is -1.29 eV , and the HOMO–LUMO gap is 4.60 eV . Compounds **naphthamide 6C–8C** exhibit similar orbital distributions and identical energy gaps to **naphthamide 9C**, as they differ only in the length of the alkane tail. Consequently, their orbital distributions are not explicitly shown.

Similarly, for compound **benzamide 9C**, both the HOMO and LUMO are localized on the dimethylaniline moiety and the amide group, with no contribution from the aliphatic tail. The HOMO, LUMO, and energy gap for 6d are -5.27 eV , -0.32 eV , and 4.94 eV , respectively. These results align with chemical intuition. In both molecules, the conjugated system, along with the amide group, serves as the most effective electron-donating and electron-withdrawing region. During interactions with the Fe surface, the amide group and the aromatic system are anticipated to be the most reactive sites.

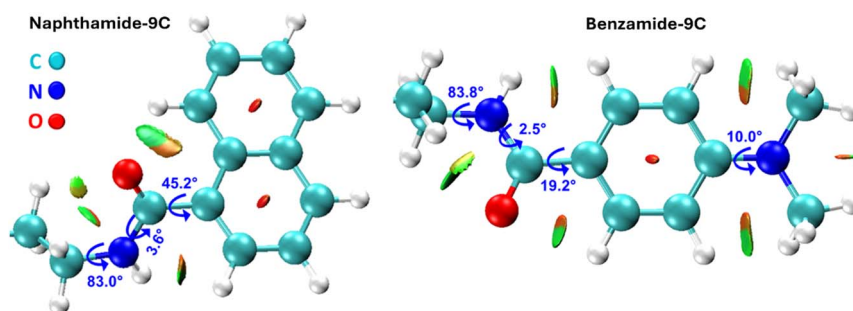


Fig. 5 Optimized structures of compounds **naphthamide 9C** and **benzamide 9C** calculated at the B3LYP-D3(BJ)/6-31G(d) level. Key structural parameters are annotated in the figure. Intramolecular interactions, analyzed using the Multiwfn program, are based on geometries optimized at the same computational level. van der Waals interactions are represented by green surfaces.

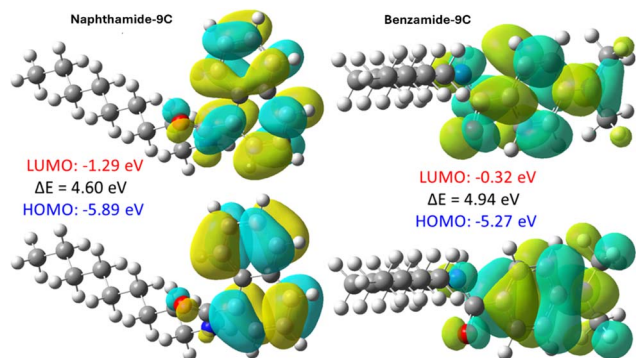


Fig. 6 Distribution of the HOMO and LUMO for compounds **naphthamide 9C** and **benzamide 9C**, along with their corresponding energies, computed at the B3LYP-D3(BJ)/6-31G(d) level.

Furthermore, the molecular electrostatic potential (MESP) map is a widely utilized tool for identifying nucleophilic and electrophilic sites within a molecule. On the MESP map, regions of low electron density (electrophilic sites) are represented by blue coloration, while regions of high electron density (nucleophilic sites) are indicated by red coloration. Neutral regions are depicted in white. Fig. 7 presents the MESP analysis of compounds **naphthamide 9C** and **benzamide 9C**, highlighting surface maxima and minima. The maxima correspond to points with the highest positive electrostatic potential (ESP), whereas the minima represent points with the most negative ESP. This analysis identifies the most electrophilic and nucleophilic regions within the molecules. In both compounds, the highest negative potential is localized around the carbonyl group, with values of $-43 \text{ kcal mol}^{-1}$ for **naphthamide 9C** and $-47 \text{ kcal mol}^{-1}$ for **benzamide 9C**. Compound **benzamide 9C** exhibits slightly greater nucleophilicity compared to **naphthamide 9C**, attributed to the extended conjugation in the naphthalene ring, which distributes electron density and reduces the electron density around the carbonyl group. The red coloration around the aromatic rings in both molecules arises from the presence of π electrons. The most electrophilic region

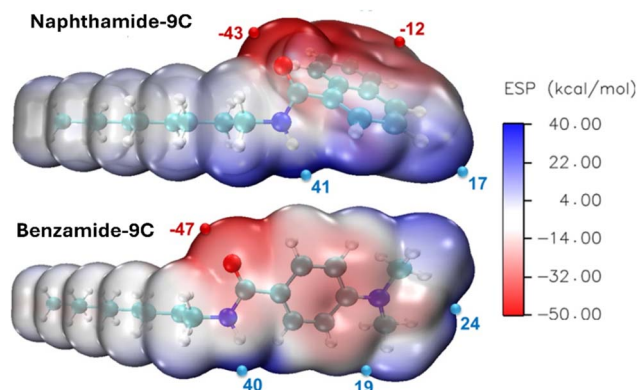


Fig. 7 Molecular electrostatic potential (MESP) surface map of compounds **naphthamide 9C** and **benzamide 9C**, displaying electrostatic potential maxima (positive values) and minima (negative values), calculated at the B3LYP-D3(BJ)/6-31G(d) level.

in both molecules is the hydrogen atom of the amide group, with a positive ESP of approximately 40 kcal mol^{-1} . These findings indicate that the carbonyl ($\text{C}=\text{O}$) and amide $\text{N}-\text{H}$ groups are the primary nucleophilic and electrophilic sites, respectively. Consequently, interactions with the metal surface are expected to predominantly involve these two functional groups and the aromatic system, with minimal contribution from the aliphatic side chain.

2.4.2 Formation of a protective coat. To date, our investigation has focused solely on individual isolated compounds, neglecting the role of intermolecular forces. Strong intermolecular interactions can cause molecules to aggregate into dimers or larger assemblies, which can form a protective layer on the metal surface, shielding it from corrosive agents. The stability and effectiveness of this protective layer are directly influenced by the strength of the intermolecular forces between the inhibitor molecules. The DFT calculations, incorporating dispersion corrections, are a widely used method for studying noncovalent interactions between molecules. In this part, DFT was employed to examine the attractive forces between inhibitor molecules and their aggregation propensity. Neither inhibitor exhibits intramolecular hydrogen bonding. As shown in Fig. 5, the only intramolecular interactions present are van der Waals forces. However, both compounds can form intermolecular hydrogen bonds *via* the amide group, facilitating the formation of an extended molecular layer on the metal surface. To investigate this, geometry optimization of the dimers of **naphthamide 9C** and **benzamide 9C** was performed using DFT at the same computational level. Multiple binding geometries were evaluated, and those with the strongest binding energies were selected. Fig. 8 illustrates the optimized geometries and reduced density gradient (RDG) plots of the dimers for both inhibitors. The analysis reveals the formation of a single hydrogen bond between the two molecules, represented by a blue surface between the oxygen atom of one molecule and the $\text{N}-\text{H}$ group of the other. Additionally, significant van der Waals interactions are observed between the molecules in the dimer. The calculated binding energies for the dimers are $60.8 \text{ kcal mol}^{-1}$ for **naphthamide 9C** and $59.4 \text{ kcal mol}^{-1}$ for **benzamide 9C**, indicating a strong tendency for both inhibitors to aggregate and form a stable protective layer on the metal surface. The dimer of **naphthamide 9C** is more stable than that of **benzamide 9C**, primarily due to stronger $\pi-\pi$ stacking interactions facilitated by the naphthalene ring in **naphthamide 9C**, compared to the benzene ring in **benzamide 9C**. These results suggest that **naphthamide 9C** may exhibit slightly superior inhibitory performance compared to **benzamide 9C**.

The global reactivity descriptors for compounds **naphthamide 9C** and **benzamide 9C** were computed using DFT calculations to evaluate their reactivity. These descriptors were derived from the energies of HOMO and LUMO.⁶¹ Generally, molecules with higher HOMO energies (E_{HOMO}) exhibit enhanced electron-donating capabilities, while lower LUMO energies (E_{LUMO}) indicate a greater capacity to accept electrons from the metal surface. Consequently, inhibitors with high E_{HOMO} and low E_{LUMO} values are expected to exhibit stronger interactions with the metal surface and higher inhibition



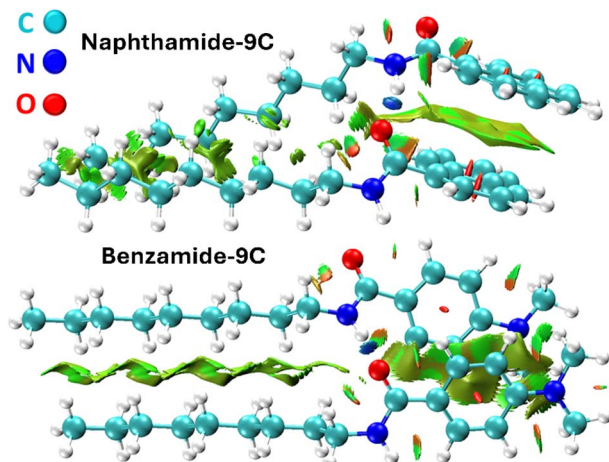


Fig. 8 The optimized geometry of the dimers of molecules **naphthamide 9C** and **benzamide 9C** optimized at the B3LYP-D3(BJ)/6-31G(d) level. Intermolecular interactions are depicted as follows: blue color indicates a hydrogen bond, green surface for van der Waals interactions, and red for rings.

efficiency. The energy gap (ΔE) between E_{HOMO} and E_{LUMO} provides insight into the inhibitor's efficiency, with smaller gaps correlating with higher reactivity and better inhibitory performance. Table 3 presents the calculated global reactivity descriptors for compounds **naphthamide 9C** and **benzamide 9C**. Both inhibitors exhibit comparable ionization potentials ($\text{IP} = -E_{\text{HOMO}}$) and electron affinities ($\text{EA} = -E_{\text{LUMO}}$), with nearly identical HOMO–LUMO energy gaps. Molecules with low IP (high E_{HOMO}) are strong electron donors, while those with low EA (low E_{LUMO}) are effective electron acceptors. Compound **benzamide 9C**, with a higher E_{HOMO} , demonstrates superior electron-donating ability compared to **naphthamide 9C**, whereas **naphthamide 9C**, with a lower E_{LUMO} , acts as a better electron acceptor. Additionally, compound **naphthamide 9C** exhibits slightly higher reactivity due to its smaller energy gap (ΔE). These results align with the molecular electrostatic potential (MESP) analysis shown in Fig. 7, where compound **naphthamide 9C** displays the most electrophilic region and **benzamide 9C** the most nucleophilic region. A smaller ΔE indicates greater polarizability and a stronger tendency to adsorb onto the metal surface, suggesting that **naphthamide 9C** is a more effective inhibitor than **benzamide 9C**. Further, chemical hardness (η) is inversely related to chemical reactivity, with higher hardness values corresponding to lower reactivity

and reduced inhibitory effectiveness. Compound **naphthamide 9C** exhibits lower hardness compared to **benzamide 9C**, further supporting its higher reactivity. The electronegativity (χ) of **benzamide 9C** is 2.79 eV, which is 0.8 eV lower than that of **naphthamide 9C**, indicating that **naphthamide 9C** has a greater ability to withdraw electrons from the filled d-orbitals of iron (Fe) and adhere more strongly to the metal surface. In summary, the calculated parameters—including HOMO, LUMO, ΔE , chemical hardness, electronegativity, and maximum charge transfer are consistent and collectively indicate that **naphthamide 9C** is a slightly more efficient inhibitor for Fe than **benzamide 9C**. These computational findings agree with experimental observations.

2.4.3 Protonated forms. Both **naphthamide 9C** and **benzamide 9C** have O and N atoms. These heteroatoms are known for their tendency to be protonated in acidic media. Molecule **naphthamide 9C** has two possible sites of protonation: O and N atoms. Fig. 7 suggests that the O atom is the most nucleophilic region in the molecule because it has the highest negative potential. Thus, the O atom is the best site for protonation. To reveal the site of protonation, geometry optimization of the O- and N-protonated forms of **naphthamide 9C** was performed and the energy of both structures was calculated using DFT. The O-protonated form was more stable by 11.1 kcal mol^{−1}. According to Maxwell–Boltzmann distribution, such a high energy difference indicates that only the O-protonated form exists. **benzamide 9C**, on the other hand, has three possible sites of protonation: two nitrogen and one oxygen atom. DFT calculations showed that the O-protonated form is more stable than the other two by more than 9 kcal mol^{−1}. Moreover, Table 3 shows a significant decrease in the energy of both HOMO and LUMO of both molecules upon protonation. The rest of the reactivity descriptors change profoundly as well. Thus, both forms are expected to show different behavior. These results confirm the importance of studying the electronic structure of the protonated forms in addition to the neutral ones. The neutral forms are better electron donors, while the protonated ones are better acceptors. Both protonated forms are more polar and more chemically reactive (have smaller ΔE) than the neutral ones. The electronegativity of the neutral **naphthamide 9C** and **benzamide 9C** are 3.59 and 2.79 eV. The electronegativity of Fe (110) is 4.82 eV.⁶² Fe is more electronegative than both neutral inhibitors, and thus electrons will transfer from the inhibitor to the metal surface. The electronegativity of the protonated forms, on the other hand, are much higher than that of Fe. This reflects the high tendency of both protonated forms to attract

Table 3 Calculated properties for molecules **naphthamide 9C** and **benzamide 9C** and their protonated forms (**naphthamide 9C–H** and **benzamide 9C–H**) at the B3LYP-D3(BJ)/6-31G(d) level, including dipole moment (Debye), energies of the HOMO and LUMO, HOMO–LUMO energy gap (ΔE), ionization potential (IP), electron affinity (EA), chemical hardness (η), chemical potential (μ), electronegativity (χ), electrophilicity index (ω), and maximum charge transfer (ΔN_{max}). All quantities, except dipole moments, are reported in electron volts (eV)

Comp.	Dipole	E_{HOMO}	E_{LUMO}	ΔE	IP	EA	η	μ	χ	ω	ΔN_{max}
Naphthamide 9C	3.2	−5.89	−1.29	4.60	5.89	1.29	2.30	−3.59	3.59	2.80	1.56
Benzamide 9C	4.9	−5.27	−0.32	4.94	5.27	0.32	2.47	−2.79	2.79	1.58	1.13
Naphthamide 9C–H	12.3	−9.58	−5.73	3.85	9.58	5.73	1.93	−7.65	7.65	15.20	3.97
Benzamide 9C–H	14.9	−8.93	−5.39	3.54	8.93	5.39	1.77	−7.16	7.16	14.49	4.05



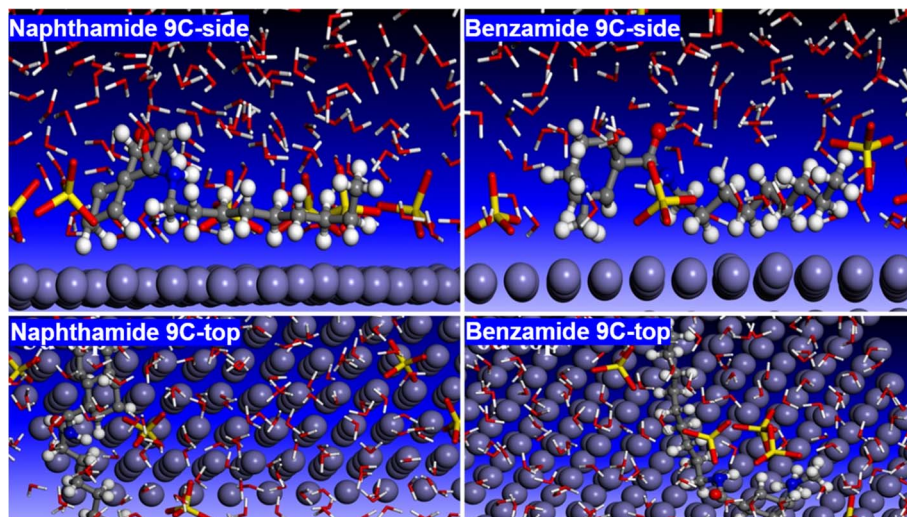


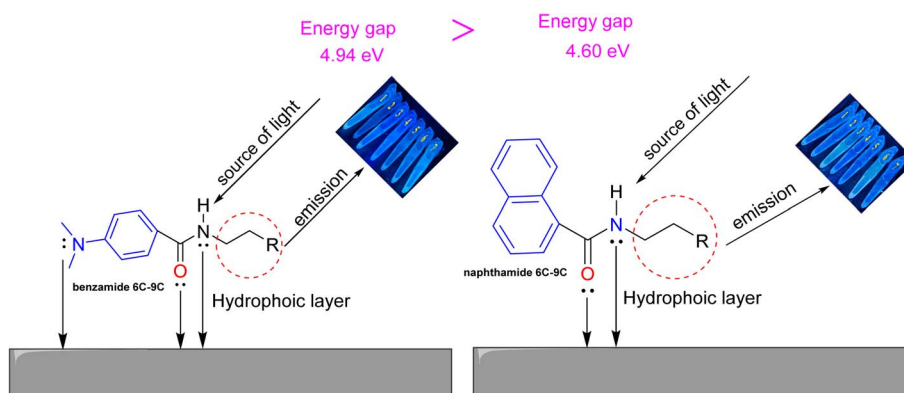
Fig. 9 Side and top views of the adsorption of naphthamide 9C and benzamide 9C on the Fe (110) surface in aqueous solution at the end of MD simulations of 1 ns.

the electrons of the d-orbital from the metal surface. The protonated form of naphthamide 9C has a higher electronegativity than benzamide 9C, and thus will have a stronger interaction with Fe. The amount of electrons transferred from the surface of the metal to the protonated inhibitor can be calculated from the Pearson theory as:⁶³ $\Delta N = (\chi_{\text{inhibitor}} - \chi_{\text{Fe}}) / 2(\eta_{\text{inhibitor}} + \eta_{\text{Fe}})$.

ΔN for naphthamide 9C and benzamide 9C are 0.57 and 0.51 electrons. These numbers show that both inhibitors have strong interactions (charge transfer) with the surface of the metal and naphthamide 9C has a slightly higher inhibition efficiency than benzamide 9C.

2.4.4 MD simulations. Molecular dynamics (MD) simulations were conducted to study the dynamic behavior of both inhibitors on the iron (Fe) surface. A simulation box was constructed containing a Fe slab, an inhibitor molecule, sulfuric acid, and water molecules. Fig. 9 illustrates the top and side views of the adsorption configurations of compounds naphthamide 9C and benzamide 9C on the Fe surface after 1 nano-second (ns) of MD simulations. The results reveal that, as the

simulation progresses, the inhibitor molecules adopt a nearly horizontal orientation on the metal surface. This configuration effectively blocks access of water and sulfuric acid molecules to the metal surface, as demonstrated in the side views of Fig. 9. Strong interactions between the inhibitor molecules and the Fe surface anchor the inhibitors in place, while the hydrophobic nature of the long alkyl chains prevents the inhibitors from migrating into the hydrophilic solvent. These findings confirm the formation of a protective adsorbed layer of inhibitors on the Fe surface, shielding it from corrosive attack by the acidic medium. Both DFT calculations and MD simulations indicate that compounds naphthamide 9C and benzamide 9C are effective inhibitors for Fe. The key functional regions in both molecules are the amide group and the aromatic rings, which correspond to the locations of the HOMO (electron-donating region) and LUMO (electron-accepting region). These groups facilitate strong interactions with the Fe surface through electron donation and acceptance. Additionally, the hydrophobic alkyl chains enhance the inhibitors' affinity for the metal surface by repelling them from the polar solvent. This aligns



Scheme 2 Suggested mechanism for the adsorption of *N*-alkyl-2-naphthamides (naphthamide 6C–9C) and 4-(dimethylamino)-*N*-alkylbenzamides (benzamide 6C–9C) on the surface of iron metal.



with experimental observations, as inhibitors with longer alkyl chains exhibit higher inhibition efficiency compared to those with shorter chains.

2.5. Mechanism of corrosion inhibition

As outlined in Scheme 2. The adsorption of investigated amides can be attributed to the presence of amide group which consider as electron donations source such as nitrogen and oxygen and aryl group which have π -electrons of aromatic ring.^{64,65} The mechanism displays the interaction between the amides and the surface of the metal through coordination bond between unshared electrons of both oxygen and nitrogen atoms as well as π -electrons of both naphthalene and benzene moieties. In addition, the presence of alkyl group can form a hydrophobic layer which able to be coated on the metal surface⁶⁶. Interestingly, all the synthesized amides exhibited emission behavior in different solvents which can form emissive layer as indicator for the coated layer of the inhibitors. DFT calculations confirmed the suggested mechanism, while Fe is more electronegative than both neutral inhibitors, and thus electrons will transfer from the inhibitor to the metal surface. The regions with the highest electron density (highest negative potential on Fig. 3) will have the strongest interaction with the Fe surface. Namely, the lone pairs of oxygen and nitrogen. However, the protonated inhibitor will accept electrons from metal to their LUMO orbital.

3. Conclusion

This research involved the synthesis and characterization of two series of amide compounds, *N*-alkyl-2-naphthamides (**naphthamide 6C–9C**) and 4-(dimethylamino)-*N*-alkylbenzamides (**benzamide 6C–9C**), through a DCC/HOBt-mediated coupling reaction. The synthesized amides demonstrated notable corrosion inhibition capabilities for mild steel in a 1.0 M H₂SO₄ solution, with compounds **naphthamide 6C–9C** achieving inhibition efficiencies of up to 80%. The superior performance of **naphthamide 6C–9C** is linked to their higher molecular weights and extended alkyl chains, which enhance surface coverage and adsorption on the metal. These conclusions were reinforced by significant shifts in corrosion potential and reductions in corrosion current densities. Furthermore, photophysical analyses revealed pronounced solvatochromic effects in the compounds. The DFT calculations offered deeper insights into the electronic characteristics and adsorption mechanisms of the inhibitors. Compound **naphthamide 9C** has a smaller HOMO–LUMO energy gap than **benzamide 9C**, which indicates that it is more reactive and is a more efficient inhibitor. DFT calculations also showed that **naphthamide 9C** is better in forming a protective layer on the surface of the metal than **benzamide 9C**. Molecular dynamics (MD) simulations showed the tendency of both inhibitors to attached itself to the surface of the metal and protect it from the corrosive assault of the acid. Both experimental and theoretical studies consistently demonstrate that compounds **naphthamide 6C–9C** are more effective corrosion inhibitors than compounds **6a–d**. The experimental data showing higher inhibition efficiencies for **naphthamide 6C–9C** are supported by the theoretical

findings of more favorable electronic properties and better adsorption behavior.

4. Experimental

4.1. General procedures for synthesis of *N*-alkyl-1-naphthamides (**naphthamide 6C–9C**)

A mixture of 2-naphthoic acid (1 g, 5.80 mmol) and primary aliphatic amine (1 equiv., 5.80 mmol) were dissolved in DMF (10 ml) then DCC (1.2 equiv., 1.438 g, 6.96 mmol) and 1-hydroxybenzotriazole (1.11 equiv., 0.941 g, 6.44 mmol) were added, then the resulting solution was stirred for 12 h at room temperature. A white precipitate formed, which was filtered off and the remaining solution was poured onto ice-water mixture, the formed precipitate was collected, dried, and recrystallized from diluted ethanol.

4.1.1 *N*-hexyl-2-naphthamides (naphthamide 6C**).** A white precipitate was obtained in 80% yield. ¹H NMR (400 MHz, DMSO-*d*₆) δ (ppm): 0.87 (t, 3H, CH₃), 1.30 (m, 6H, 3CH₂), 1.56 (m, 2H, CH₂), 3.30 (t, 2H, CH₂NH), 7.59 (m, 2H, ArH), 7.97 (m, 4H, ArH), 8.44 (s, 1H, ArH), 8.61 (t, 1H, NH). ¹³C NMR (100 MHz, DMSO-*d*₆) δ (ppm): 13.93 (CH₃), 22.08 (CH₂), 26.22 (CH₂), 29.13 (CH₂), 31.05 (CH₂NH), 124.19 (Ar), 126.05 (Ar), 126.65 (Ar), 127.26 (Ar), 127.44 (Ar), 127.58 (Ar), 127.77 (Ar), 132.09 (Ar), 132.16 (Ar), 134.03 (Ar), 166.08 (C=O).

4.1.2 *N*-heptyl-2-naphthamide (naphthamide 7C**).** A white precipitate was obtained in 75% yield. ¹H NMR (400 MHz, DMSO-*d*₆) δ (ppm): 0.86 (t, 3H, CH₃), 1.26 (m, 4H, 2CH₂), 1.31 (m, 2H, 2CH₂), 1.57 (m, 2H, CH₂), 3.31 (t, 2H, CH₂NH), 7.60 (m, 2H, ArH), 7.98 (m, 4H, ArH), 8.45 (s, 1H, ArH), 8.62 (t, 1H, NH). ¹³C NMR (100 MHz, DMSO-*d*₆) δ (ppm): 13.95 (CH₃), 22.08 (CH₂), 26.51 (CH₂), 28.49 (CH₂), 29.16 (CH₂), 31.26 (CH₂NH), 124.19 (Ar), 126.05 (Ar), 127.26 (Ar), 127.44 (Ar), 127.58 (Ar), 127.77 (Ar), 128.78 (Ar), 132.09 (Ar), 132.16 (Ar), 134.03 (Ar), 166.08 (C=O).

4.1.3 *N*-octyl-2-naphthamide (naphthamide 8C**).** A white precipitate was obtained in 78% yield. ¹H NMR (400 MHz, DMSO-*d*₆) δ (ppm): 0.85 (t, 3H, CH₃), 1.25 (m, 6H, 3CH₂), 1.31 (m, 4H, 2CH₂), 1.57 (m, 2H, CH₂), 3.30 (t, 2H, CH₂NH), 7.60 (m, 2H, ArH), 7.97 (m, 4H, ArH), 8.44 (s, 1H, ArH), 8.61 (t, 1H, NH). ¹³C NMR (100 MHz, DMSO-*d*₆) δ (ppm): 13.95 (CH₃), 22.10 (CH₂), 26.55 (CH₂), 28.68 (CH₂), 28.79 (CH₂), 29.15 (CH₂), 31.27 (CH₂NH), 124.19 (Ar), 126.65 (Ar), 127.26 (Ar), 127.44 (Ar), 127.58 (Ar), 127.77 (Ar), 128.78 (Ar), 132.09 (Ar), 132.16 (Ar), 134.03 (Ar), 166.08 (C=O).

4.1.4 *N*-nonyl-2-naphthamide (naphthamide 9C**).** A white precipitate was obtained in 82% yield. ¹H NMR (400 MHz, DMSO-*d*₆) δ (ppm): 0.85 (t, 3H, CH₃), 1.24 (m, 12H, 6CH₂), 1.56 (m, 2H, CH₂), 3.30 (t, 2H, CH₂NH), 7.60 (m, 2H, ArH), 7.97 (m, 4H, ArH), 8.45 (s, 1H, ArH), 8.61 (t, 1H, NH).

4.2. General procedures for synthesis of 4-(dimethylamino)-*N*-alkylbenzamides (**benzamide 6C–9C**)

A mixture of 4-(dimethylamino) benzoic acid (1 g, 6.05 mmol) and primary aliphatic amines (1 equiv., 6.05 mmol) were dissolved in DMF (10 ml) then DCC (1.2 equiv., 1.49 g, 7.26 mmol)

and 1-hydroxybenzotriazole (1.11 equiv., 0.981 g, 6.71 mmol) were added, and the reaction mixture was stirred for 12 h at room temperature. A white precipitate formed, which was filtered off and the remaining solution was poured onto ice-water mixture, the formed precipitate was collected, dried, and recrystallized from diluted ethanol.

4.2.1 4-(Dimethylamino)-N-hexyl benzamide (benzamide 6C). A white precipitate was collected in 82% yield. ^1H NMR (400 MHz, DMSO- d_6) δ (ppm): 0.86 (t, 3H, CH_3), 1.25 (m, 6H, 3CH_2), 1.27 (m, 6H, 3CH_2), 1.49 (m, 2H, CH_2), 2.95 (s, 6H, $2\text{CH}_3\text{-N}$), 3.22 (t, 2H, CH_2NH), 6.67 (d, 2H, ArH), 7.70 (d, 2H, ArH), 8.06 (t, 1H, NH). ^{13}C NMR (100 MHz, DMSO- d_6) δ (ppm): 14.16 (CH_3), 22.30 (CH_2), 26.44 (CH_2), 29.58 (CH_2), 31.30 (CH_2NH), 40.15 (CH_3N), 110.95 (Ar), 121.71 (Ar), 128.63 (Ar), 152.15 (Ar), 166.16 (C=O).

4.2.2 4-(Dimethylamino)-N-heptyl benzamide (benzamide 7C). A white precipitate was collected in 75% yield. ^1H NMR (400 MHz, DMSO- d_6) δ (ppm): 0.86 (t, 3H, CH_3), 1.27–1.71 (m, 10H, 5CH_2), 1.27 (m, 6H, 3CH_2), 1.49 (m, 2H, CH_2), 2.95 (s, 6H, $2\text{CH}_3\text{-N}$), 3.21 (t, 2H, CH_2NH), 6.67 (d, 2H, ArH), 7.70 (d, 2H, ArH), 8.07 (t, 1H, NH). ^{13}C NMR (100 MHz, DMSO- d_6) δ (ppm): 14.13 (CH_3), 22.29 (CH_2), 26.43 (CH_2), 29.57 (CH_2), 31.29 (CH_2NH), 40.15 (CH_3N), 110.95 (Ar), 121.70 (Ar), 128.62 (Ar), 152.16 (Ar), 166.14 (C=O).

4.2.3 4-(Dimethylamino)-N-octylbenzamide (benzamide 8C). A white precipitate was collected in 85% yield. ^1H NMR (400 MHz, DMSO- d_6) δ (ppm): 0.85 (t, 3H, CH_3), 1.26–1.49 (m, 12H, 6CH_2), 2.95 (s, 6H, $2\text{CH}_3\text{-N}$), 3.19 (t, 2H, CH_2NH), 6.67 (d, 2H, ArH), 7.70 (d, 2H, ArH), 8.06 (t, 1H, NH). ^{13}C NMR (100 MHz, DMSO- d_6) δ (ppm): 14.16 (CH_3), 22.31 (CH_2), 26.77 (CH_2), 28.91 (CH_2), 29.02 (CH_2), 29.60 (CH_2), 31.48 (CH_2NH), 40.15 (CH_3N), 110.95 (Ar), 121.70 (Ar), 128.62 (Ar), 152.16 (Ar), 166.14 (C=O).

4.2.4 4-(Dimethylamino)-N-nonylbenzamide (benzamide 9C). A white precipitate was collected in 80% yield. ^1H NMR (400 MHz, DMSO- d_6) δ (ppm): 0.85 (t, 3H, CH_3), 1.24–1.71 (m, 14H, 7CH_2), 2.95 (s, 6H, $2\text{CH}_3\text{-N}$), 3.19 (t, 2H, CH_2NH), 6.67 (d, 2H, ArH), 7.70 (d, 2H, ArH), 8.06 (t, 1H, NH). ^{13}C NMR (100 MHz, DMSO- d_6) δ (ppm): 14.16 (CH_3), 22.31 (CH_2), 26.75 (CH_2), 28.89 (CH_2), 29.05 (CH_2), 29.20 (CH_2), 29.58 (CH_2), 31.50 (CH_2NH), 40.15 (CH_3N), 110.95 (Ar), 121.69 (Ar), 128.62 (Ar), 152.15 (Ar), 166.13 (C=O).

Data availability

Mostafa Sayed and Mostafa Ahmed, the corresponding authors and all the coauthors, confirm that all the data associated with this article is available in the main article and ESI.†

Conflicts of interest

The authors state that there are no conflicts to declare.

Acknowledgements

The authors express their gratitude for the substantial computing resources provided by the Digital Research Alliance of Canada. They also extend their thanks to Professor De-Qi

Yuan, a Professor of Pharmaceutical Chemistry at the Faculty of Pharmacy, Kobe Gakuin University, Japan, for his assistance and support in facilitating NMR analysis measurements.

References

- 1 M. M. H. Imran, S. Jamaludin and A. F. Mohamad Ayob, A critical review of machine learning algorithms in maritime, offshore, and oil & gas corrosion research: A comprehensive analysis of ANN and RF models, *Ocean Eng.*, 2024, **295**, 116796, DOI: [10.1016/j.oceaneng.2024.116796](https://doi.org/10.1016/j.oceaneng.2024.116796).
- 2 A. Sharma, J. Kaur and A. Saxena, Anti-corrosive Properties of Synthetic Organic Compounds: A Review, *J. Bio-Tribo-Corros.*, 2024, **10**, 80, DOI: [10.1007/s40735-024-00884-8](https://doi.org/10.1007/s40735-024-00884-8).
- 3 F. M. Galleguillos Madrid, *et al.*, Green Corrosion Inhibitors for Metal and Alloys Protection in Contact with Aqueous Saline, *Materials*, 2024, **17**, 1–20.
- 4 H.-M. Yang, Role of Organic and Eco-Friendly Inhibitors on the Corrosion Mitigation of Steel in Acidic Environments—A State-of-Art Review, *Molecules*, 2021, **26**.
- 5 L. Guo, *et al.*, Electrochemical and surface investigations of N, S codoped carbon dots as effective corrosion inhibitor for mild steel in acidic solution, *Colloids Surf., A*, 2024, **702**, 135062, DOI: [10.1016/j.colsurfa.2024.135062](https://doi.org/10.1016/j.colsurfa.2024.135062).
- 6 S. Ren, M. Cui, X. Chen, S. Mei and Y. Qiang, Comparative study on corrosion inhibition of N doped and N,S codoped carbon dots for carbon steel in strong acidic solution, *J. Colloid Interface Sci.*, 2022, **628**, 384–397, DOI: [10.1016/j.jcis.2022.08.070](https://doi.org/10.1016/j.jcis.2022.08.070).
- 7 Z. Chen, *et al.*, Highly Biodegradable Corrosion Inhibitors Derived from Sunflower Oil for Mild Steel Corrosion in CO_2 - and H_2S -Saturated Oilfield-Produced Water, *Energy Fuels*, 2024, **38**, 9529–9545, DOI: [10.1021/acs.energyfuels.4c01684](https://doi.org/10.1021/acs.energyfuels.4c01684).
- 8 S. Fu, *et al.*, A comprehensive study of highly soluble cationic polyfluorene as a polymer anticorrosive coating: Anticorrosion mechanisms and performance evaluation, *Prog. Org. Coat.*, 2024, **191**, 108455, DOI: [10.1016/j.porgcoat.2024.108455](https://doi.org/10.1016/j.porgcoat.2024.108455).
- 9 J. Luo, *et al.*, The effect of N and S ratios in N, S co-doped carbon dot inhibitor on metal protection in 1 M HCl solution, *J. Taiwan Inst. Chem. Eng.*, 2021, **127**, 387–398, DOI: [10.1016/j.jtice.2021.08.023](https://doi.org/10.1016/j.jtice.2021.08.023).
- 10 A. Ashwathareddy, *et al.*, Corrosion mitigation of mild steel in acidic medium using liquid crystals: A comprehensive review, *Inorg. Chem. Commun.*, 2024, **169**, 113071, DOI: [10.1016/j.inoche.2024.113071](https://doi.org/10.1016/j.inoche.2024.113071).
- 11 E. Berdimurodov, *et al.*, Green β -cyclodextrin-based corrosion inhibitors: Recent developments, innovations and future opportunities, *Carbohydr. Polym.*, 2022, **292**, 119719, DOI: [10.1016/j.carbpol.2022.119719](https://doi.org/10.1016/j.carbpol.2022.119719).
- 12 M. Mahdavian and S. Ashhari, Mercapto functional azole compounds as organic corrosion inhibitors in a polyester-melamine coating, *Prog. Org. Coat.*, 2010, **68**, 259–264, DOI: [10.1016/j.porgcoat.2010.04.002](https://doi.org/10.1016/j.porgcoat.2010.04.002).
- 13 Nikhil, G. Ji and R. Prakash, Composites of Donor- π -Acceptor type configured organic compound and porous



- ZnO nano sheets as corrosion inhibitors of copper in chloride environment, *J. Mol. Liq.*, 2019, **280**, 160–172, DOI: [10.1016/j.molliq.2019.02.026](https://doi.org/10.1016/j.molliq.2019.02.026).
- 14 B. Sanyal, Organic compounds as corrosion inhibitors in different environments — A review, *Prog. Org. Coat.*, 1981, **9**, 165–236, DOI: [10.1016/0033-0655\(81\)80009-X](https://doi.org/10.1016/0033-0655(81)80009-X).
 - 15 M. S. S. Carranza, Y. I. A. Reyes, E. C. Gonzales, D. P. Arcon and F. C. Franco, Electrochemical and quantum mechanical investigation of various small molecule organic compounds as corrosion inhibitors in mild steel, *Heliyon*, 2021, **7**, e07952, DOI: [10.1016/j.heliyon.2021.e07952](https://doi.org/10.1016/j.heliyon.2021.e07952).
 - 16 A. K. Al-Edan, *et al.*, Palmitic acid-based amide as a corrosion inhibitor for mild steel in 1M HCl, *Heliyon*, 2023, **9**, e14657, DOI: [10.1016/j.heliyon.2023.e14657](https://doi.org/10.1016/j.heliyon.2023.e14657).
 - 17 J. Cruz, R. Martínez, J. Genesca and E. García-Ochoa, Experimental and theoretical study of 1-(2-ethylamino)-2-methylimidazoline as an inhibitor of carbon steel corrosion in acid media, *J. Electroanal. Chem.*, 2004, **566**, 111–121, DOI: [10.1016/j.jelechem.2003.11.018](https://doi.org/10.1016/j.jelechem.2003.11.018).
 - 18 A. M. Elsharif, S. A. Abubshait, I. Abdulazeez and H. A. Abubshait, Synthesis of a new class of corrosion inhibitors derived from natural fatty acid: 13-Docosenoic acid amide derivatives for oil and gas industry, *Arabian J. Chem.*, 2020, **13**, 5363–5376, DOI: [10.1016/j.arabjc.2020.03.015](https://doi.org/10.1016/j.arabjc.2020.03.015).
 - 19 R. S. Abdel Hameed, M. Alfakeer and M. Abdallah, Inhibiting Properties of Some Heterocyclic Amide Derivatives as Potential Nontoxic Corrosion Inhibitors for Carbon Steel in 1.0 M Sulfuric Acid, *Surf. Eng. Appl. Electrochem.*, 2018, **54**, 599–606, DOI: [10.3103/S1068375518060054](https://doi.org/10.3103/S1068375518060054).
 - 20 A. S. Fouda, H. S. El-Desoky, M. M. Abdel-Galeil and D. Mansour, Amide Compounds as Corrosion Inhibitors for Carbon Steel in Acidic Environment, *Protect. Met. Phys. Chem. Surface*, 2022, **58**, 151–167, DOI: [10.1134/S2070205122010105](https://doi.org/10.1134/S2070205122010105).
 - 21 S. S. Sam, *et al.*, Peptide immobilisation on porous silicon surface for metal ions detection, *Nanoscale Res. Lett.*, 2011, **6**, 412, DOI: [10.1186/1556-276X-6-412](https://doi.org/10.1186/1556-276X-6-412).
 - 22 H. Sun, *et al.*, Amide group enhanced self-assembly and adsorption of dicarboxylic amino acid surfactants on a rhodochrosite surface through intermolecular weak interaction, *Sep. Purif. Technol.*, 2023, **309**, 122905, DOI: [10.1016/j.seppur.2022.122905](https://doi.org/10.1016/j.seppur.2022.122905).
 - 23 Q. Sun, *et al.*, Amide group enhanced self-assembly and adsorption of thioether-containing hydroxamic acid on cassiterite surface, *AIChE J.*, 2023, **69**, e18023, DOI: [10.1002/aic.18023](https://doi.org/10.1002/aic.18023).
 - 24 X. Ma, *et al.*, Synthesis, experimental and theoretical studies of triazine derivatives with surface activity as effective corrosion inhibitors for medium carbon steel in acid medium, *J. Mol. Liq.*, 2020, **315**, 113711, DOI: [10.1016/j.molliq.2020.113711](https://doi.org/10.1016/j.molliq.2020.113711).
 - 25 D. S. Chauhan, C. Verma and M. A. Quraishi, Molecular structural aspects of organic corrosion inhibitors: Experimental and computational insights, *J. Mol. Struct.*, 2021, **1227**, 129374, DOI: [10.1016/j.molstruc.2020.129374](https://doi.org/10.1016/j.molstruc.2020.129374).
 - 26 J.-J. Liu, *et al.*, Cocrystals of naphthalene diimide with naphthalene derivatives: A facile approach to tune the luminescent properties, *Dyes Pigm.*, 2018, **149**, 59–64, DOI: [10.1016/j.dyepig.2017.09.058](https://doi.org/10.1016/j.dyepig.2017.09.058).
 - 27 R. Irshad, S. Asim, A. Mansha and Y. Arooj, Naphthalene and its Derivatives: Efficient Fluorescence Probes for Detecting and Imaging Purposes, *J. Fluoresc.*, 2023, **33**, 1273–1303, DOI: [10.1007/s10895-023-03153-y](https://doi.org/10.1007/s10895-023-03153-y).
 - 28 C. Verma, E. E. Ebenso, M. A. Quraishi and K. Y. Rhee, Phthalocyanine, naphthalocyanine and their derivatives as corrosion inhibitors: A review, *J. Mol. Liq.*, 2021, **334**, 116441, DOI: [10.1016/j.molliq.2021.116441](https://doi.org/10.1016/j.molliq.2021.116441).
 - 29 L. Wang, Y.-L. Liu and M.-S. Wang, Effects of Atypical Hydrogen Bonds and π - π Interactions on Nonlinear Optical Properties: Dimers of Triangular Structures Based on Perylene, Naphthalene, and Pyromellitic Diimides, *Langmuir*, 2023, **39**, 357–366, DOI: [10.1021/acs.langmuir.2c02594](https://doi.org/10.1021/acs.langmuir.2c02594).
 - 30 J. Li, *et al.*, Describing curved-planar π - π interactions: modeled by corannulene, pyrene and coronene, *Phys. Chem. Chem. Phys.*, 2013, **15**, 12694–12701, DOI: [10.1039/C3CP51095F](https://doi.org/10.1039/C3CP51095F).
 - 31 X. Chen, S. M. Argandona, F. Melle, N. Rampal and D. Fairen-Jimenez, Advances in surface functionalization of next-generation metal-organic frameworks for biomedical applications: Design, strategies, and prospects, *Chem*, 2024, **10**, 504–543, DOI: [10.1016/j.chempr.2023.09.016](https://doi.org/10.1016/j.chempr.2023.09.016).
 - 32 A. Q. Ramle, E. R. T. Tiekink and W. J. Basirun, Synthesis, functionalization and coordination chemistry of dibenzotetraaza[14]annulenes, *Coord. Chem. Rev.*, 2022, **469**, 214672, DOI: [10.1016/j.ccr.2022.214672](https://doi.org/10.1016/j.ccr.2022.214672).
 - 33 K. Wieszczycka, *et al.*, Surface functionalization – The way for advanced applications of smart materials, *Coord. Chem. Rev.*, 2021, **436**, 213846, DOI: [10.1016/j.ccr.2021.213846](https://doi.org/10.1016/j.ccr.2021.213846).
 - 34 J. B. Lee, *et al.*, Annulative π -Extension of Unactivated Benzene Derivatives through Nondirected C–H Arylation, *Org. Lett.*, 2019, **21**, 7004–7008, DOI: [10.1021/acs.orglett.9b02583](https://doi.org/10.1021/acs.orglett.9b02583).
 - 35 M. Finšgar and J. Jackson, Application of corrosion inhibitors for steels in acidic media for the oil and gas industry: A review, *Corros. Sci.*, 2014, **86**, 17–41, DOI: [10.1016/j.corsci.2014.04.044](https://doi.org/10.1016/j.corsci.2014.04.044).
 - 36 Y. Qin, G. Li, T. Qi and H. Huang, Aromatic imide/amide-based organic small-molecule emitters for organic light-emitting diodes, *Mater. Chem. Front.*, 2020, **4**, 1554–1568, DOI: [10.1039/D0QM00084A](https://doi.org/10.1039/D0QM00084A).
 - 37 O. Younis, A. F. Al-Hossainy, M. Sayed, A. M. Kamal El-dean and M. S. Tolba, Synthesis and intriguing single-component white-light emission from oxadiazole or thiadiazole integrated with coumarin luminescent core, *J. Photochem. Photobiol., A*, 2022, **431**, 113992, DOI: [10.1016/j.jphotochem.2022.113992](https://doi.org/10.1016/j.jphotochem.2022.113992).
 - 38 M. S. Tolba, A. M. Sayed, M. Sayed and M. Ahmed, Design, synthesis, biological evaluation, and molecular docking of some new Thieno[2,3-d] pyrimidine derivatives, *J. Mol. Struct.*, 2021, **1246**, 131179, DOI: [10.1016/j.molstruc.2021.131179](https://doi.org/10.1016/j.molstruc.2021.131179).
 - 39 A. A. Abozeed, *et al.*, Combined experimental and TD-DFT/DMO3 investigations, optical properties, and



- photoluminescence behavior of a thiazolopyrimidine derivative, *Sci. Rep.*, 2022, **12**, 15674, DOI: [10.1038/s41598-022-19840-y](https://doi.org/10.1038/s41598-022-19840-y).
- 40 M. Li, *et al.*, Current trends in the detection and removal of heavy metal ions using functional materials, *Chem. Soc. Rev.*, 2023, **52**, 5827–5860, DOI: [10.1039/D2CS00683A](https://doi.org/10.1039/D2CS00683A).
 - 41 D.-X. Xue, Q. Wang and J. Bai, Amide-functionalized metal-organic frameworks: Syntheses, structures and improved gas storage and separation properties, *Coord. Chem. Rev.*, 2019, **378**, 2–16, DOI: [10.1016/j.ccr.2017.10.026](https://doi.org/10.1016/j.ccr.2017.10.026).
 - 42 S. Gonta, *et al.*, Fluorescent substituted amidines of benzanthrone: Synthesis, spectroscopy and quantum chemical calculations, *Spectrochim. Acta, Part A*, 2013, **101**, 325–334, DOI: [10.1016/j.saa.2012.09.104](https://doi.org/10.1016/j.saa.2012.09.104).
 - 43 V. Arun, *et al.*, The tautomerism, solvatochromism and non-linear optical properties of fluorescent 3-hydroxyquinoxaline-2-carboxalidine-4-aminoantipyrine, *Dyes Pigm.*, 2010, **87**, 149–157, DOI: [10.1016/j.dyepig.2010.03.012](https://doi.org/10.1016/j.dyepig.2010.03.012).
 - 44 A. Varghese and K. B. Akshaya in *Reviews in Fluorescence 2017*, ed. C. D. Geddes, Springer International Publishing, 2018, pp. 99–121.
 - 45 G. Das, *et al.*, Fluorescence turn on amine detection in a cationic covalent organic framework, *Nat. Commun.*, 2022, **13**, 3904, DOI: [10.1038/s41467-022-31393-2](https://doi.org/10.1038/s41467-022-31393-2).
 - 46 E. Khezerloo, S. M. Mousavi-khosdel and V. Safarifar, Sensitive and selective detection of metal ions and small molecules in aqueous media using a hydrolytically stable amide-functionalized metal-organic framework, *Polyhedron*, 2019, **166**, 166–174, DOI: [10.1016/j.poly.2019.03.049](https://doi.org/10.1016/j.poly.2019.03.049).
 - 47 Z. Ma, F. E. Jacobsen and D. P. Giedroc, Coordination chemistry of bacterial metal transport and sensing, *Chem. Rev.*, 2009, **109**, 4644–4681, DOI: [10.1021/cr900077w](https://doi.org/10.1021/cr900077w).
 - 48 C. Panda, A. Sarkar and S. Sen Gupta, Coordination chemistry of carboxamide 'Nx' ligands to metal ions for bio-inspired catalysis, *Coord. Chem. Rev.*, 2020, **417**, 213314, DOI: [10.1016/j.ccr.2020.213314](https://doi.org/10.1016/j.ccr.2020.213314).
 - 49 H.-Y. Ma, *et al.*, An amide groups functionalized Cd-MOF as multi-responsive luminescent sensor for detecting Fe³⁺, Cr₂O₇²⁻ and OTC in water media, *J. Mol. Struct.*, 2023, **1291**, 136009, DOI: [10.1016/j.molstruc.2023.136009](https://doi.org/10.1016/j.molstruc.2023.136009).
 - 50 S. Heng, A. M. Mak, D. B. Stubing, T. M. Monro and A. D. Abell, Dual Sensor for Cd(II) and Ca(II): Selective Nanoliter-Scale Sensing of Metal Ions, *Anal. Chem.*, 2014, **86**, 3268–3272, DOI: [10.1021/ac500619z](https://doi.org/10.1021/ac500619z).
 - 51 Z. Wang, S. Cui, S. Qiu and S. Pu, A dual-functional fluorescent sensor based on diarylethene for Zn²⁺ and Al³⁺ in different solvents, *J. Photochem. Photobiol. A*, 2019, **376**, 185–195, DOI: [10.1016/j.jphotochem.2019.03.020](https://doi.org/10.1016/j.jphotochem.2019.03.020).
 - 52 F.-J. Huo, *et al.*, A rhodamine-based dual chemosensor for the visual detection of copper and the ratiometric fluorescent detection of vanadium, *Dyes Pigm.*, 2010, **86**, 50–55, DOI: [10.1016/j.dyepig.2009.11.007](https://doi.org/10.1016/j.dyepig.2009.11.007).
 - 53 A. M. Shams El Din and N. J. Paul, Oxide film thickening on some molybdenum-containing stainless steels used in desalination plants, *Desalination*, 1988, **69**, 251–260, DOI: [10.1016/0011-9164\(88\)80028-6](https://doi.org/10.1016/0011-9164(88)80028-6).
 - 54 M. Ahmed, *et al.*, Synthesis of Novel Biocompatible Thienopyrimidine Chromophores with Aggregation-Induced Emission Sensitive to Molecular Aggregation, *ACS Omega*, 2020, **5**, 29988–30000, DOI: [10.1021/acsomega.0c04358](https://doi.org/10.1021/acsomega.0c04358).
 - 55 K. I. Aly, *et al.*, Conducting copolymers nanocomposite coatings with aggregation-controlled luminescence and efficient corrosion inhibition properties, *Prog. Org. Coat.*, 2019, **135**, 525–535, DOI: [10.1016/j.porgcoat.2019.06.001](https://doi.org/10.1016/j.porgcoat.2019.06.001).
 - 56 O. Younis, M. Abdel-Hakim, M. M. Sayed, O. Tsutsumi and K. I. Aly, Liquid crystal polymers as luminescent coatings: Single-component white-light photoluminescence and corrosion inhibition, *J. Lumin.*, 2021, **239**, 118361, DOI: [10.1016/j.jlumin.2021.118361](https://doi.org/10.1016/j.jlumin.2021.118361).
 - 57 H. Maeda, T. Maeda and K. Mizuno, Absorption and Fluorescence Spectroscopic Properties of 1- and 1,4-Silyl-Substituted Naphthalene Derivatives, *Molecules*, 2012, **17**, 5108–5125.
 - 58 D. Braun, W. Rettig, S. Delmond, J. F. Létard and R. Lapouyade, Amide Derivatives of DMABN: A New Class of Dual Fluorescent Compounds, *J. Phys. Chem. A*, 1997, **101**, 6836–6841, DOI: [10.1021/jp970168f](https://doi.org/10.1021/jp970168f).
 - 59 C. Reichardt, Solvatochromic Dyes as Solvent Polarity Indicators, *Chem. Rev.*, 1994, **94**, 2319–2358, DOI: [10.1021/cr00032a005](https://doi.org/10.1021/cr00032a005).
 - 60 S. Gómez, E. N. Soysal and G. A. Worth, Micro-Solvated DMABN: Excited State Quantum Dynamics and Dual Fluorescence Spectra, *Molecules*, 2021, **26**.
 - 61 A. S. M. Gad El-hak, A. A. K. Mohammed, A. F. Abdel Hakiem and R. M. Mahfouz, Molecular conformation, vibrational spectroscopic and NBO analysis of atenolol and atenolol-hydrochlorothiazide cocrystals, *Spectrochim. Acta, Part A*, 2019, **222**, 117200, DOI: [10.1016/j.saa.2019.117200](https://doi.org/10.1016/j.saa.2019.117200).
 - 62 A. Kokalj, On the HSAB based estimate of charge transfer between adsorbates and metal surfaces, *Chem. Phys.*, 2012, **393**, 1–12, DOI: [10.1016/j.chemphys.2011.10.021](https://doi.org/10.1016/j.chemphys.2011.10.021).
 - 63 R. G. Parr and R. G. Pearson, Absolute hardness: companion parameter to absolute electronegativity, *J. Am. Chem. Soc.*, 1983, **105**, 7512–7516, DOI: [10.1021/ja00364a005](https://doi.org/10.1021/ja00364a005).
 - 64 I. Ahamad, R. Prasad and M. A. Quraishi, Inhibition of mild steel corrosion in acid solution by Pheniramine drug: Experimental and theoretical study, *Corros. Sci.*, 2010, **52**, 3033–3041, DOI: [10.1016/j.corsci.2010.05.022](https://doi.org/10.1016/j.corsci.2010.05.022).
 - 65 E. E. El-Katori, M. Ahmed and H. Nady, Imidazole derivatives based on glycourils as efficient anti-corrosion inhibitors for copper in HNO₃ solution: Synthesis, electrochemical, surface, and theoretical approaches, *Colloids Surf., A*, 2022, **649**, 129391, DOI: [10.1016/j.colsurfa.2022.129391](https://doi.org/10.1016/j.colsurfa.2022.129391).
 - 66 A. M. Hegazy, N. S. Haiba, M. K. Awad and F. M. Mahgoub, Synthesis, DFT, molecular dynamics, and Monte Carlo simulation of a novel thiourea derivative with extraordinary inhibitive properties for mild steel in 0.5 M sulphuric acid, *Phys. Chem. Chem. Phys.*, 2023, **25**, 9532–9547, DOI: [10.1039/D3CP00139C](https://doi.org/10.1039/D3CP00139C).

